

Targeted observations based on sensitive areas identified by CNOP to improve the thermal structure predictions in the summer Yellow Sea: operation in the field

Kun Liu¹, Wuhong Guo¹, Lianglong Da², Jingyi Liu¹, Huiqin Hu¹, and Baolong Cui¹

¹Qingdao National Laboratory for Marine Science and Technology

²Navy Submarine Academy

November 24, 2022

Abstract

Targeted observation is an appealing procedure for improving model predictions through the assimilation of additional collected measurements. However, studies on targeted observations in the oceanic field have been largely based on modeling efforts, and there is a need for field validating operations. Here, we report the results of a field program that is designed based on the sensitive areas identified by the Conditional Nonlinear Optimal Perturbation (CNOP) approach to improve the short-range (7 days) summer thermal structure prediction in the Yellow Sea. We found good spatial consistency in the locations of the identified sensitive areas among the hindcast and climatology runs. By introducing the technique of cycle data assimilation and the new concept of time-varying sensitive areas, we designed an observing strategy based on the identified sensitive areas, and conducted a set of Observing System Simulation Experiments prior to assessing the effectiveness of the plan on later observations. On this basis, the impact of targeted observations was investigated by a choreographed field campaign in the summer of 2019. The results of the in-field Observing System Experiments show that compared to conventional local data assimilation, conducting targeted observations in sensitive areas can double the benefits of data assimilation in thermal structure prediction. Furthermore, dynamic analysis demonstrates that the refinement of vertical thermal structures is mainly caused by the changes in the upstream horizontally advected temperature driven by the Yellow Sea Cold Water Mass circulation. This study highlights the effectiveness of targeted observations on reducing the forecast uncertainty in the ocean.

1 **Targeted observations based on sensitive areas identified by CNOP to improve the**
2 **thermal structure predictions in the summer Yellow Sea: operation in the field**

3

4 **Kun Liu^{1,2}, Wuhong Guo^{1,2}, Lianglong Da^{1,2,*}, Jingyi Liu^{1,2}, Huiqin Hu², Baolong Cui^{1,2}**

5 ¹Navy Submarine Academy, Qingdao, China

6 ²Qingdao National Laboratory for Marine Science and Technology, Qingdao, China

7

8 Corresponding author: Lianglong Da (da_lianglong@126.com)

9

10 **Key Points:**

- 11 • We first extend the scope of oceanic targeted observation to summer thermal structure
12 prediction;
- 13 • We propose the observation strategy with a new concept of time-varying sensitive areas;
- 14 • We validate the benefit of the oceanic targeted observation in the actual field operation
15 guided by the identified sensitive areas.

16

17 **Abstract**

18 Targeted observation is an appealing procedure for improving model predictions through the
19 assimilation of additional collected measurements. However, studies on targeted observations in
20 the oceanic field have been largely based on modeling efforts, and there is a need for field
21 validating operations. Here, we report the results of a field program that is designed based on the
22 sensitive areas identified by the Conditional Nonlinear Optimal Perturbation (CNOP) approach
23 to improve the short-range (7 days) summer thermal structure prediction in the Yellow Sea. We
24 found good spatial consistency in the locations of the identified sensitive areas among the
25 hindcast and climatology runs. By introducing the technique of cycle data assimilation and the
26 new concept of time-varying sensitive areas, we designed an observing strategy based on the
27 identified sensitive areas, and conducted a set of Observing System Simulation Experiments
28 prior to assessing the effectiveness of the plan on later observations. On this basis, the impact of
29 targeted observations was investigated by a choreographed field campaign in the summer of
30 2019. The results of the in-field Observing System Experiments show that compared to
31 conventional local data assimilation, conducting targeted observations in sensitive areas can
32 double the benefits of data assimilation in thermal structure prediction. Furthermore, dynamic
33 analysis demonstrates that the refinement of vertical thermal structures is mainly caused by the
34 changes in the upstream horizontally advected temperature driven by the Yellow Sea Cold Water
35 Mass circulation. This study highlights the effectiveness of targeted observations on reducing the
36 forecast uncertainty in the ocean.

37

38 **1. Introduction**

39 The predictability of oceanic processes is limited since the ocean is an extremely complex
40 dynamic system (Mu et al., 2017). The uncertainty of ocean forecasting can be reduced through
41 the assimilation of observation data (Oke et al., 2015). Unlike observations on land, field-
42 deployed oceanic observations are scarce and expensive. Thus, maximizing the individual
43 impact of these limited measurements is a meaningful pursuit. Targeted observation is believed
44 to be a suitable strategy for solving this problem (Farrara et al., 2013; Lermusiaux, 2007; Li et
45 al., 2014; Majumdar, 2016).

46 Interest in the field of oceanic targeted observation has accelerated over the past few years
47 (Baehr et al., 2008; Köhl & Stammer, 2004; Krama et al., 2012; Li et al., 2014; Morss & Battisti,
48 2004; Wang et al., 2013; Zhang et al., 2019). Morss & Battisti (2004) evaluated the effects of
49 different numbers and locations of oceanic observations on the prediction of the El Niño-South
50 Oscillation (ENSO) based on a series of Observing System Simulation Experiments (OSSEs).
51 Baehr et al. (2008) studied the effects of different observing systems on the monitoring of the
52 meridional overturning circulation in the North Atlantic. Krama et al. (2012) investigated the
53 optimal observation locations for improving the predictability of the Kuroshio Extension. Li et
54 al. (2014) reported an improvement in ocean prediction when utilizing targeted observations in
55 the South China Sea (SCS) western boundary current region. Zhang et al. (2019) designed and
56 evaluated a targeted observation network for improving upstream Kuroshio transport prediction.
57 These studies confirmed the effectiveness of oceanic targeted observation; however, most of the
58 relevant studies have been largely based on modeling efforts, and experiments in the field are
59 necessary regarding both method validation and the cost-effectiveness evaluation.

60 A limited number of oceanic targeted observations in real scenarios have been reported in
61 the literature (Curtin & Bellingham, 2009; Mourre & Alvarez, 2012; Shay et al., 2011). Curtin &
62 Bellingham (2009) implemented the Autonomous Ocean Sampling Network (AOSN) field
63 program in Monterey Bay and demonstrated that proper sampling is critical for both
64 understanding and predicting ocean fields. To predict the local ocean circulation and potential
65 pathways of spilled oil, Shay et al. (2011) carried out oceanographic surveys based on the
66 positions of the exploded oil rig and the loop currents in the Gulf of Mexico. They found that the
67 root-mean-square errors (RMSEs) of the simulated results were reduced by approximately 30%
68 when the additional measurements were assimilated into the hindcast model. Guided by the
69 optimal designed glider trajectory, which sets the trace of the error covariance matrix as criteria
70 (Alvarez & Mourre, 2012), Mourre & Alvarez (2012) found that the data assimilation
71 performance of the adaptive-sampling-driven glider data was better than that of the independent
72 glider data in the same region, with an RMSE reduction of 18%.

73 However, none of the abovementioned in-field oceanic targeted observations were designed
74 based on identified “sensitive areas”. Given a certain phenomenon, sensitive areas are the
75 specific localized areas that are expected to contribute most in reducing the prediction

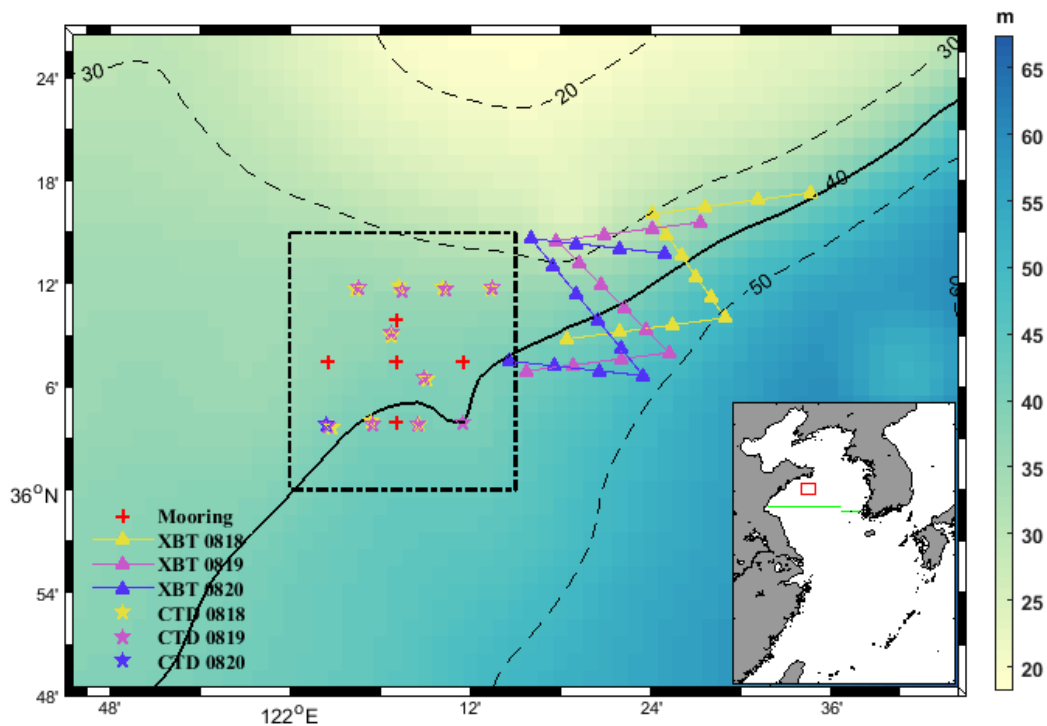
76 uncertainties in the target region. In a study of storm tracking prediction, Montani et al. (1999)
77 demonstrated that short-range prediction refinement can be increased from an average of 15% to
78 approximately 37% if the observations are deployed in sensitive areas. Targeted observation
79 studies in the atmospheric field started earlier and are more mature than those in the ocean.
80 Among others, the Atlantic observing-system research and predictability experiment
81 (THORPEX) is a remarkable program that concluded that targeting and assimilating
82 observations in sensitive areas are effective in improving forecasts (Majumdar, 2016).
83 Nevertheless, tests of targeted observations guided by identified sensitive areas in real at-sea
84 scenarios are still lacking.

85 The identification of the sensitive areas is a crucial step in targeted observations (Majumdar,
86 2016; Zhang et al., 2017). The sensitive areas for targeted observation can be identified by the
87 Conditional Nonlinear Optimal Perturbation (CNOP) approach proposed by Mu et al. (2003).
88 Utilizing the CNOP approach, the optimal initial errors that cause the largest nonlinear forecast
89 uncertainty can be calculated, and their spatial patterns help to locate the sensitive areas. To date,
90 CNOP-identified sensitive areas have been proven to be quite effective in a number of oceanic
91 applications, such as the prediction of the ENSO (Duan & Hu, 2016), upstream Kuroshio
92 transport (Zhang et al., 2017), Kuroshio intrusion into the SCS (Liang et al., 2019), Kuroshio
93 large meander (Wang et al., 2013), the ocean state in the SCS western boundary current region
94 (Li et al., 2014). However, when focusing on a specific oceanic motion or event, there are many
95 detailed issues to be addressed, e.g., the determination of the objective function and the
96 constraint of the initial errors, the design of the optimal observation strategy and the
97 determination of the effectiveness of the targeted observations in the field operation.

98 In the present study, we first extend the scope of oceanic targeted observations to
99 summertime thermal structure predictions in a coastal sea, and put them into effect by
100 conducting an oceanographic investigation in the field. We select temperature as the target
101 variable because of its predominant impact on density fields and acoustic propagation (Dushaw
102 et al., 2013). Under the comprehensive impact of the thermodynamic and dynamic oceanic
103 processes and topography, the thermal structures in the coastal sea feature significant spatial and
104 temporal variations, and their forecast uncertainty is generally large (Xia et al., 2006).
105 Identifying the sensitive areas for the selected target region may enhance our understanding of

106 the physical mechanism responsible for the thermal structure variation. In addition, exploring the
 107 utility of targeted observations in the thermal structure prediction may help improve the regional
 108 forecast system, with an optimally designed monitoring system deployed in the sensitive area.
 109 Here, we focus on improving the 7-day thermal structure prediction in the specified target region
 110 in the northwest Yellow Sea (YS; see locations in Figure 1). We found that assimilating the
 111 observations in the identified sensitive areas is more effective than locally assimilating
 112 approximately equal number of measurements inside the target region.

113 The article is organized as follows: The model configuration, the CNOP approach and the
 114 assimilation technique are briefly described in section 2. In section 3, given a specified target
 115 region, the sensitive areas for thermal structure prediction are identified. Then, the observation
 116 strategies are designed and quantitatively assessed by conducting a series of OSSEs. Section 4
 117 introduces the observational data obtained from the ocean hydrographic survey and presents the
 118 improvements in the thermal structure prediction due to the targeted observation through
 119 Observing System Experiments (OSEs). The physical mechanism behind signal transport is also
 120 discussed. The results are summarized in section 5.



122 **Figure 1.** Plan view of the locations of the five temperature profile buoy stations (red
123 crosses), thirty-six XBT stations (triangles), and twenty-one shipboard CTD stations (stars). The
124 differences in the deployment times of the XBT and shipboard CTD observations are
125 distinguished by different colors. The black dashed box indicates the location of the target
126 region. The topography is indicated by shading. The bottom-right insert shows the model area, in
127 which the red box indicates the position of the study area and the green lines indicate the section
128 locations used for vertical thermal structure validation.

129 **2. Methodology**

130 **2.1 Numerical model configuration**

131 To investigate the utility of targeted observation in improving the prediction of thermal
132 structures in the shallow YS, the Regional Ocean Modeling System (ROMS) solving the three-
133 dimensional Reynolds-averaged hydrostatic Navier-Stokes equation with the Boussinesq
134 approximation was used (Shchepetkin & McWilliams, 2005). The ROMS utilizes a nonlinear
135 terrain-following vertical coordinate and has been proven to be suitable for regional ocean
136 modeling by an increasing number of studies (Liang et al., 2019; Liu et al., 2019; Yang et al.,
137 2011; Zhang et al., 2017). The K-profile parameterization scheme is used to calculate the vertical
138 eddy viscosity and diffusivity (Large et al. 1994). Harmonic horizontal mixing is employed with
139 constant horizontal eddy viscosity and diffusivity of $10 \text{ m}^2\text{s}^{-1}$ and $15 \text{ m}^2\text{s}^{-1}$, respectively. The
140 bottom stress is parameterized following a quadratic formula with a constant bottom drag
141 coefficient set to 2.5×10^{-3} .

142 The model region covers the China Seas north of 23.7°N (Figure 1, $23.7\text{-}41.3^\circ\text{N}$, 117-
143 132.5°E) with $1/24^\circ$ horizontal resolution, and there are 32 vertical levels that are unevenly
144 distributed, with closer spacing within the range of stratification. The model topography is
145 subsampled from ETOPO2 (<https://ngdc.noaa.gov/mgg/global/etopo2>), and the minimum water
146 depth is set to 10 m. The model initial temperature and salinity are obtained from the multiyear
147 averaged (1998-2018) HYCOM+NCODA reanalysis data (<https://www.hycom.org/dataserver>) in
148 January. The initial current velocities and sea surface height are set to zero.

149 First, a climatology run is carried out from a cold start. At the open boundaries, the model is
 150 driven by the multiyear averaged monthly HYCOM+NCODA reanalysis data and tidal forcing of
 151 eight major tidal constituents (M_2 , S_2 , K_1 , O_1 , N_2 , K_2 , P_1 , and Q_1). The tidal forcing is included at
 152 the open boundaries by the Flather condition (Flather, 1976) with the tidal elevation and
 153 barotropic velocity obtained from the global inverse barotropic tidal model TPXO7.2 (Egbert &
 154 Erofeeva, 2002). On the surface, the wind stress, surface heat flux and water exchange are
 155 calculated from the multiyear averaged (1998-2018) monthly ECMWF reanalysis data
 156 (<https://apps.ecmwf.int/datasets/>). The climatology run is integrated for 25 years for spin-up.

157 Thereafter, a hindcast run is conducted from January 2014 to August 2019, starting from the
 158 results of the climatology run. Unlike the monthly mean external forcing data used for the
 159 climatology run, twelve-hourly surface forcing from the ECMWF reanalysis data and daily
 160 boundary forcing from the HYCOM+NCODA reanalysis data are applied to drive the hindcast
 161 run. The hindcast run is also forced by tidal forcing (eight major constituents) from TPXO7.2. In
 162 this paper, the daily-averaged temperature profiles are used for analysis.

163 2.2 CNOP approach

164 In this section, we briefly review the CNOP approach (Mu et al., 2003; 2009). Let M_t be
 165 the nonlinear propagator that propagates the value \mathbf{X}_0 at initial time t_0 to $\mathbf{X}_t = M_t(\mathbf{X}_0)$ at the
 166 end of the forecast time. When adding the initial perturbation $\Delta\mathbf{x}_0$ to the initial state, the
 167 nonlinear evolution of the initial perturbation $\Delta\mathbf{x}_t$ can be expressed as

$$168 \quad \Delta\mathbf{x}_t = M_t(\mathbf{X}_0 + \Delta\mathbf{x}_0) - M_t(\mathbf{X}_0), \quad (1)$$

169 Following the definition proposed by Mu et al. (2003), the CNOP can be obtained by
 170 solving the following nonlinear constraint maximization problem:

$$171 \quad J(\Delta\mathbf{x}_{0,\sigma}) = \max_{\|\Delta\mathbf{x}_0\| \leq \sigma} J(\Delta\mathbf{x}_0) = \max_{\|\Delta\mathbf{x}_0\| \leq \sigma} \|M_t(\mathbf{X}_0 + \Delta\mathbf{x}_0) - M_t(\mathbf{X}_0)\|, \quad (2)$$

172 with the constraint condition $\|\Delta\mathbf{x}_0\| \leq \sigma$, where $J(\Delta\mathbf{x}_0)$ is the objective function that estimates
 173 the nonlinear evolution of the initial perturbation during time t . $\|\cdot\|$ denotes the norm of the

174 vector. $\Delta \mathbf{x}_{0,\sigma}$ is the CNOP-type initial error, which will induces the largest prediction error at the
 175 prediction time t .

176 Generally, CNOP computation relies on the adjoint technique to calculate the gradient of
 177 the objective function. However, directly calculating CNOP in a complicated model requires a
 178 considerable amount of coding and is computationally expensive (Liang et al., 2019; Zhang et
 179 al., 2017). Alternatively, in this study, we use an Empirical Orthogonal Function (EOF) based
 180 algorithm proposed by Wang & Tan (2009) to approximate the CNOP without using the adjoint
 181 technique (hereafter referred to as the EOF-CNOP method). Wang & Tan (2009) tested the EOF-
 182 CNOP method in a typhoon case. They found that the sensitive areas identified by this
 183 approximation algorithm are similar to the real CNOP results but require much less
 184 computational resources. The calculation process of the EOF-CNOP method is described as
 185 follows: First, a set of initial perturbations is added to the initial state to obtain the corresponding
 186 prediction increment ensemble by numerical integration. Then, the orthogonal basis of the initial
 187 perturbation ensemble is calculated by EOF decomposition. Finally, a statistical relationship is
 188 established between the initial perturbations and the associated prediction increment; thus, the
 189 gradient of the objective function can be obtained, and the CNOP can be computed.

190 In practice, the specific form of the objective function and the initial constraint are defined
 191 according to the object of study. In the context of the thermal structure of interest in this study,
 192 the objective function is defined as the change in the volume-integrated temperature caused by
 193 the initial errors in the specified target region, such that

$$194 \quad J = \left(\int_A \Delta T_t dx dy dz \right)^2, \quad (3)$$

195 where ΔT_t indicates the temperature anomaly at the future time t caused by the initial errors and
 196 A denotes the selected target region.

197 Following the formula of Li et al. (2014), the initial constraint is defined as

$$198 \quad \|\Delta \mathbf{x}_0\|^2 = \int_D \left(\frac{\Delta T_0}{T_{std}} \right)^2 dx dy dz \leq \sigma^2, \quad (4)$$

199 where ΔT_0 indicates the initial temperature perturbation, D denotes the model domain, and T_{std}
 200 indicates the regionally averaged temperature standard deviation in the simulated domain, which
 201 is calculated from the World Ocean Atlas 2018 (WOA18,
 202 <https://www.nodc.noaa.gov/OC5/woa18/>) in August and set to 0.25°C in this study. The
 203 constraint radius σ is set to 2.5×10^3 to keep the state change in a reasonable range under the
 204 perturbation and to ensure the model stability. After completing all these steps, the sequential
 205 quadratic programming (Powell, 1983) algorithm is employed to compute the CNOP.

206 2.3 Optimal interpolation data assimilation

207 The Optimal Interpolation (OI) technique is utilized to assimilate the targeted observation
 208 data to reduce uncertainties in the initial fields, which can be formulated as

$$209 \begin{cases} x_a = x_b + K(y_{obs} - Hx_b) \\ K = BH^T (HBH^T + R)^{-1} \end{cases} \quad (5)$$

210 where x_a and x_b indicate the analysis field and background field, respectively. y_{obs} denotes the
 211 observation vector, and H is the matrix of the model background field projections converted
 212 into the observational space. K is the weight matrix, which is calculated based on H , the model
 213 background field error covariation matrix B , and the observational error covariation matrix R .
 214 R is diagonal since all the observational errors are assumed uncorrelated in space. That is,

$$215 R_{ij} = \sigma_o^2 \sigma_{ij}, \quad (6)$$

216 where σ_o is determined by the accuracies of the observations, σ_{ij} is the Kronecker delta, $\sigma_{ij} = 1$
 217 when $i = j$, and $\sigma_{ij} = 0$ when $i \neq j$. The model background field error covariation matrix B at
 218 different vertical layers is assumed to be independent. Similar to the estimation used by Zhang
 219 (2019), B_{ij} is written as follows:

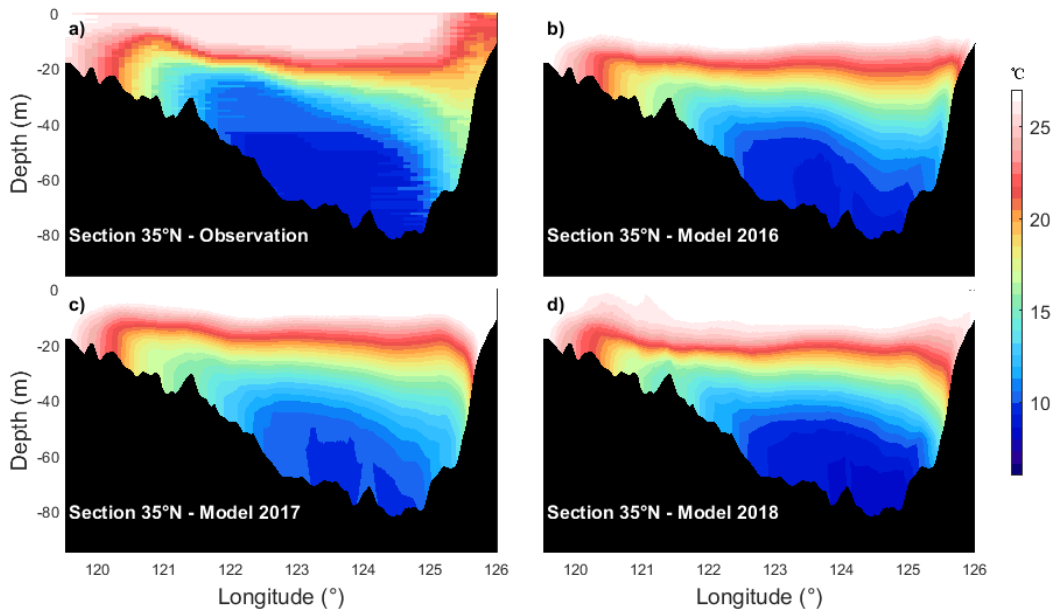
$$220 \begin{cases} B_{ij} = \sigma_b^2 \exp(-(\frac{d_{ij}}{L_c})^2) & d_{ij} \leq R_0 \\ 0 & d_{ij} > R_0 \end{cases} \quad (7)$$

221 where σ_b is determined by the initial model errors, d_{ij} is the distance between two model grid
222 points i and j . Referring to the temperature assimilation study in the YS by Ji et al. (2017), in
223 this paper, the correlation length L_c and the influence radius R_o were set to 60 km and 120 km,
224 respectively.

225 **3. Identification of the sensitive area and observation strategy design**

226 **3.1 Vertical thermal structure validation**

227 The simulated monthly averaged temperature along the section of 35°N (see location in
228 Figure 1) in the hindcast years of 2016-2018 is compared with previous observations obtained
229 from the Atlas of Ocean Data in the China Seas (Chen et al., 1992). In August, the water is
230 mixed well in very shallow regions near the coast, and is stratified in the central basin. The
231 simulated vertical distribution of isothermals is generally consistent with observations. Below the
232 thermocline, the Yellow Sea Cold Water Mass (YSCWM) that formed during the previous
233 winter is well reproduced. In the bottom, there are two cold cores inside the YSCWM, which
234 agrees with a previous observational study (Zhang et al., 2008). The vertical thermal structure
235 features interannual variability among the hindcast years, which is closely related to the
236 interannual variability of the YSCWM and surface heating (Hu & Wang, 2004). In summary, the
237 simulated vertical structure shows fairly good agreement with earlier observational and numerical
238 studies. However, there is still a margin for improvement in the accuracy of the simulated thermal
239 structure, especially below the surface mixing layer.



240

241 **Figure 2.** Comparison of the monthly mean (Aug) temperatures along section 35°N between the
 242 hindcast simulations (2016, 2017 and 2018) and the observations redrawn from the Atlas of
 243 Ocean Data in the China Seas.

244 3.2 CNOP-identified sensitive areas

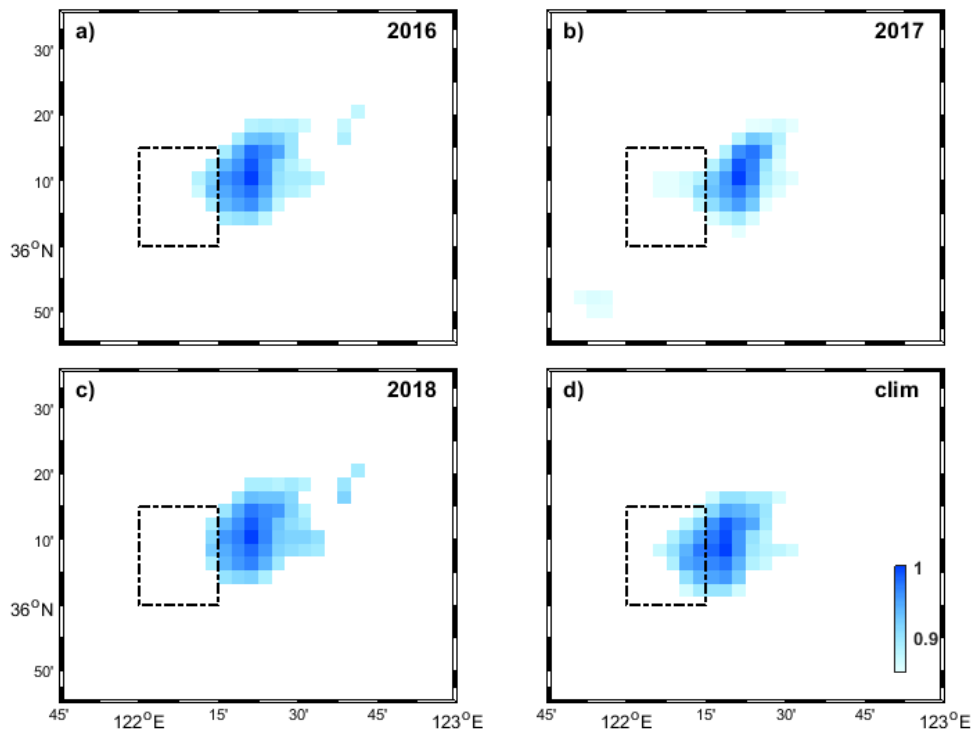
245 To provide guidance for a targeted observation field campaign, a vital step is the identification
 246 of the sensitive areas. Several previous studies have utilized CNOP-identified sensitive areas to guide
 247 preferred oceanic targeted observations (Li et al., 2014; Wang et al., 2013; Zhang et al., 2017);
 248 however, oceanic sensitive area identification has not been studied in the context of thermal
 249 structure prediction. Given a selected target region located in the southeastern of the Shandong
 250 Peninsula ($122\text{-}122.25^{\circ}\text{E}$, $36\text{-}36.25^{\circ}\text{N}$, the black dashed box in Figure 1), we aim to improve the
 251 short-term (7 days) summer thermal structure prediction by conducting targeted observations in
 252 the identified sensitive area. Considering the ships' voyage schedule, the initial prediction time is
 253 set to 00:00 on 20 August, and the daily averaged temperature profiles in the target region on 26
 254 August are used for the forecast validation.

255 Note that the identification of the sensitive areas from the real-time predicted ocean state is
 256 not attempted, as this would entail the establishment of a reliable local prediction model with
 257 forcing from a larger-scale prediction model as a prerequisite. To provide guidance for the field

258 campaign in August 2019, the sensitive areas in the last three hindcast years (2016-2018) are first
259 identified.

260 Following Wang & Tan (2009), to identify the sensitive area, in every hindcast year, an
261 ensemble of 20 initial perturbations and a natural run without perturbation is built. For this study
262 of thermal structure prediction, initial perturbations are added to the temperature, which is
263 achieved by taking the discrepancy of the daily averaged HYCOM+NCODA temperature data at
264 the targeting day (20 August) between every two adjacent years during 1998-2018. All the initial
265 temperature perturbations are scaled to the same magnitude of 0.25°C , which is estimated based
266 on the temperature standard deviations within the simulation area from the WOA18 climatology
267 data in August. Then, following the method of Zhang et al. (2017), the CNOP is calculated by
268 employing a vertically integrated temperature scheme based on the 21 sets of initial ensemble
269 conditions and the corresponding 7-day forecast samples. We confine the CNOP-identified
270 sensitive area as the region where the CNOP-type errors have vertically integrated temperatures
271 larger than a certain value τ . τ is determined to obtain a sensitive area which is the same size
272 as the target region, which contains 56 horizontal model grids in this study.

273



274

275 **Figure 3.** Locations of the identified sensitive areas for a) b) c) the hindcast years 2016-2018 and
276 d) the last climatology year. The CNOPs are all normalized according to their maximum values.

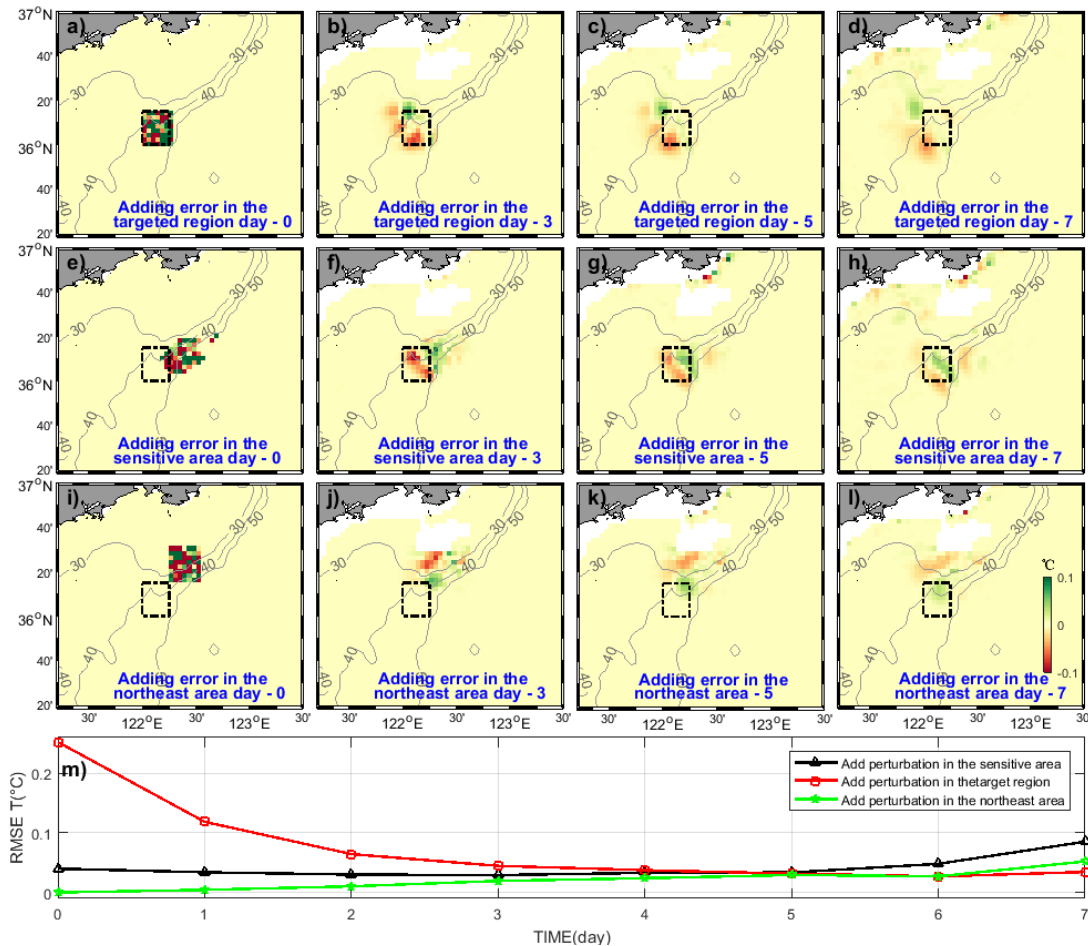
277

278 The spatial distributions of the calculated CNOPs for the last three hindcast years of 2016-
279 2018 are shown in Figures 3a-c. The absolute values of the CNOPs are different in every
280 hindcast year, but only the relative values matter in the identification of the sensitive areas; thus,
281 the CNOPs are all normalized according to their maximum values. We find that the sensitive
282 areas are mainly located outside of the target region in the northeast, with only a small fraction of
283 the area overlapping. In every hindcast year, the locations of the maximum values are generally
284 consistent. The discrepancies among the identified sensitive areas are mainly concentrated in the
285 marginal areas.

286 To validate the sensitivity in more detail, we systematically perturb the temperature fields at
287 the initial time in three different areas (the sensitive area, the target region, and the area
288 northeastern of the target region) and investigate the model responses in the temperature
289 structure simulation (quantified by the regionally averaged temperature profile RMSEs in the
290 target region). The northeast area is regarded as a nonsensitive area outside of the target region,
291 and it is of the same size as the target region for a reasonable comparison. Random temperature
292 perturbations with a normal distribution $N(0, 0.25)$ are added to all three of the above selected
293 regions. The temporal evolution of the temperature prediction errors at a depth of 20 m in 2016 is
294 shown in Figure 4. The development of the temperature perturbations is similar among the three
295 hindcast years (not shown), they move westward and southwestward along with model
296 integration. Adding perturbations in the target region causes the largest RMSEs at the initial time
297 (Figure 4m). When perturbations are added to the sensitive area, the initial RMSEs are small but
298 not zero due to the overlap with the target region. After 7 days of simulation, the RMSEs in the
299 target region become the largest (Figure 5). These results suggest that at the prediction time, the
300 local thermal structures in the target region are mostly affected by the initial perturbations in the
301 sensitive area. Thus, the current method is proven to be effective in identifying the sensitive
302 areas for the vertical thermal structures.

303 On the basis that the locations of the identified sensitive areas are generally consistent in space

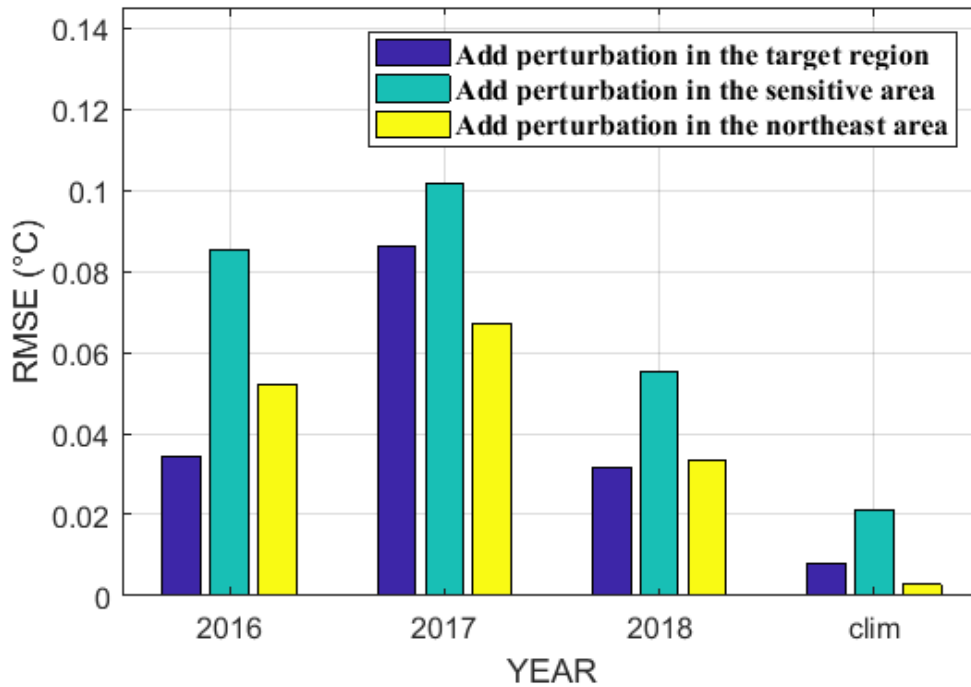
304 in every hindcast year, we try to obtain a multiyear averaged sensitive area to guide the field
 305 campaign. Following the same procedures, the sensitive area in the last climatology year is identified.
 306 The results show that the location of the identified sensitive area in the last climatology run agrees
 307 with that in the hindcast runs (Figure 3d). Perturbation experiments are also conducted in the last
 308 climatology run and confirm the effectiveness of the identified sensitive area (Figure 5). Thus,
 309 the CNOP-identified sensitive area from the last climatology run is used to guide the observation
 310 strategy designment (Figure 3d).



311

312 **Figure 4.** Temporal evolution of the temperature prediction errors at a depth of 20 m during the
 313 prediction time in 2016, with initial perturbations added to a-d) the target region, e-h) the
 314 sensitive area and i-l) the northeast area, respectively. Daily averaged results of the initial time,
 315 the third day, the fifth day and the seventh day are shown. m) Temporal evolution of the
 316 temperature RMSEs averaged in the target region.

317



318

319 **Figure 5.** Temperature profile RMSEs in the target region after 7 days of simulation for the
 320 hindcast runs and the last climatology run with random perturbations added to different areas.

321

322 3.3 Design of observation strategy and benefit assessment with Observing System 323 Simulation Experiments

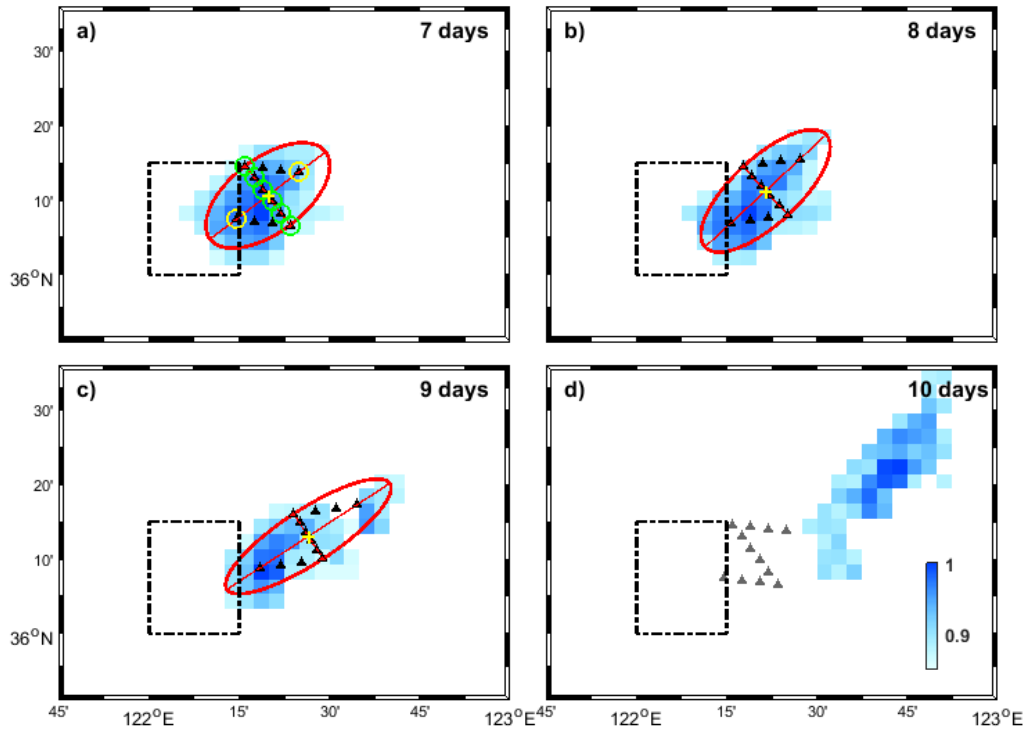
324 Before actually starting the field campaign, a targeted observation strategy that includes the
 325 ship route and the deployment locations should be designed. Moreover, the data assimilation
 326 technique (we use OI data assimilation here, section 2.3) should be utilized to maximize the
 327 benefit of the limited observation resources.

328 Three preconditions are assumed before determining the observation stations. First, a “Z”
 329 shape route is chosen to maximize the observation coverage in the identified sensitive area after
 330 conducting several numerical experiments (not shown here). Second, the daily averaged
 331 temperature observations are used for data assimilation to better represent the general vertical
 332 thermal structure. To obtain the daily average temperature profiles at each station, the ship route
 333 is designed to repeat four times a day (04:30-07:30, 10:30-13:30, 16:30-19:30, and 22:30-01:30).

334 Considering the observation simultaneity, the ship route length L is limited by the ship's speed
335 (set to 8 knots) and the sailing time to complete each path (set to 3 hours). Third, although the
336 prediction errors are expected to decrease for a higher number of observations, 12 stations are set
337 along each route (approximately 4 km between the adjacent two stations) considering both the
338 horizontal resolution (approximately 5 km) of our model and the observation cost.

339 Based on these preconditions, the specific ship route and the corresponding deployment
340 locations along it are designed as follows: First, the spatial central point of the route is
341 determined by averaging all the model grid coordinates in the sensitive area (the yellow cross in
342 Figure 6a). Then, an ellipse is fitted with the central point, a major axis A_{long} , a minor axis A_{short}
343 and a dip angle, and is scaled by a certain ratio to represent most of the sensitive area (the red
344 ellipse in Figure 6a). Next, six equally spaced stations are set along the minor axis (green circles
345 in Figure 6a). We assume that the shape “Z” is symmetric and that both ends of “Z” are located
346 on the major axis of the ellipse. Given L and A_{short} , the leading and trailing observation stations
347 on the major axis can be confirmed based on the Pythagorean theorem (yellow circles in Figure
348 6a). Finally, four equally spaced stations are added along the other two sides of the “Z” based on
349 the above determined stations (Figure 6a). Except for the westernmost station, all the designed
350 observation stations are out of the range of the target region.

351 It is worth noting that, the settings mentioned above represent a somewhat subjective
352 strategy based on several assumptions and may not be the best solution. Observation
353 optimization strategies for guiding targeting observations are urgently needed but are beyond the
354 scope of this paper and will be investigated in future studies.



355

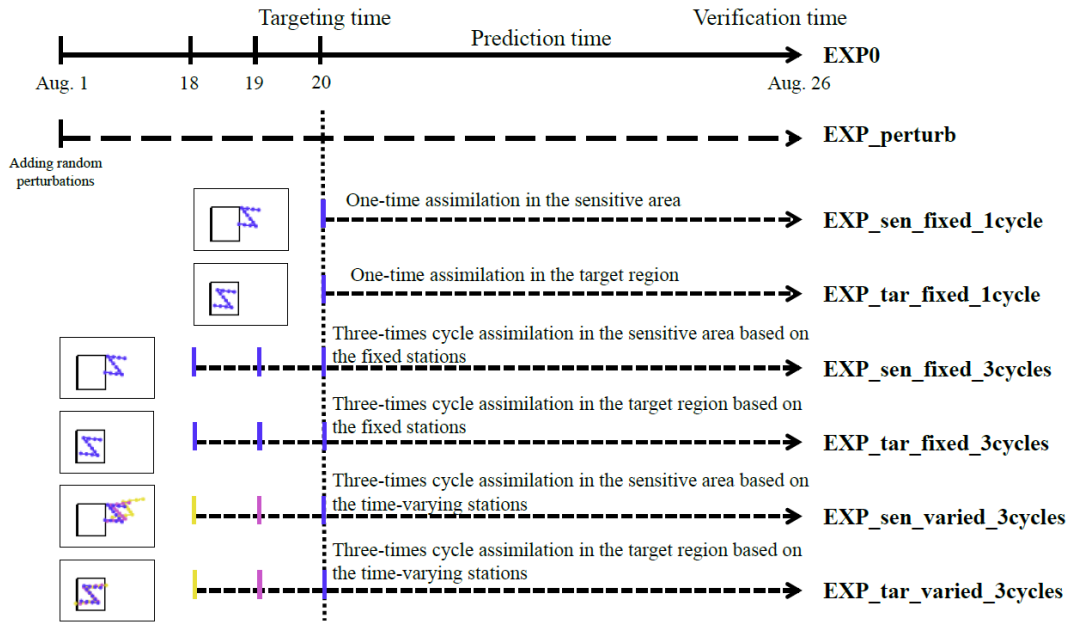
356

357

358

359

Figure 6. a) b) c) Z- shaped observation stations (black triangles) designed based on the time-varying sensitive area (background colors). The black dashed box indicates the target region. The station locations in d) (gray triangles) are the same as those in a), which are completely out of the range of the 10-day sensitive area.



360

361

362

363

364

365

366

Figure 7. Schematic diagram of the Observing System Simulation Experiments based on the last climatology run. All the assimilation experiments use the results of the natural run as synthetic observations. The assimilated data station locations and the corresponding assimilation times are plotted by the same colors.

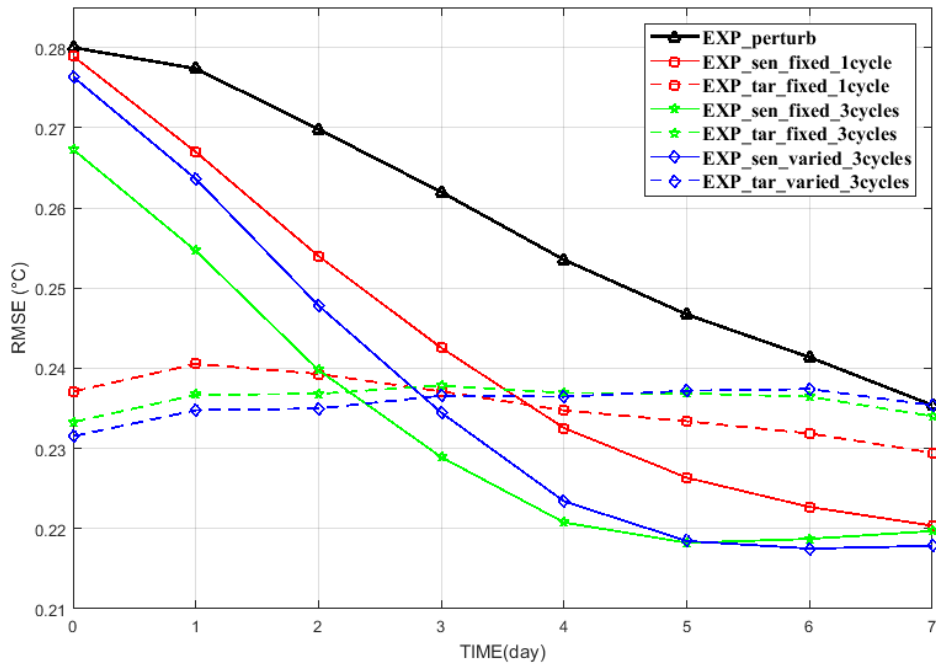
Table 1. Design of OSSEs based on the climatology run

Experiments	Data assimilation	Assimilation cycle	Comment
EXP0	no	-	Nature run
EXP_perturb	no	-	Adding perturbation at the targeting time
EXP_sen_fixed_1cycle	yes	1	One-time assimilation in the sensitive area at the stations shown in Figure6a
EXP_tar_fixed_1cycle	yes	1	One-time assimilation at the parallel stations in the target region (Figure 7)

EXP_sen_fixed_3cycles	yes	3	Three-times cycle assimilation in the sensitive area at the fixed stations (Figures 6a and 7)
EXP_tar_fixed_3cycles	yes	3	Three-times cycle assimilation at the parallel fixed stations in the target region (Figure 7)
EXP_sen_varied_3cycles	yes	3	Three-times cycle assimilation in the sensitive area at the time-varying stations (Figures 6a-c, Figure 7)
EXP_tar_varied_3cycles	yes	3	Three-times cycle assimilation at the parallel time-varying stations in the target region (Figures 7 and 10)

367

368 To evaluate the performance of the designed observation stations and the assimilation
369 system, we implement a series of OSSEs based on the simulated results of the last climatology
370 year (Table 1 and Figure 7). The original ocean state is denoted by the natural run EXP0, which
371 is considered as the synthetic observation. Then, a control experiment (EXP_perturb) is created
372 by superimposing temperature perturbations to EXP0 at 00:00, 1 August. The perturbation field
373 is chosen among the 20 initial ensemble perturbations created for sensitive area identification,
374 which induces the largest errors after 7 days of simulation. The perturbation magnitude is scaled
375 to 0.35°C, which is larger than the perturbation magnitude of 0.25°C in sensitive area
376 identification, considering the error attenuation from the beginning (1 August) to the targeting
377 time (20 August). In addition to the natural run and the control run, two assimilation experiments
378 (EXP_sen_fixed_1cycle and EXP_tar_fixed_1cycle) are conducted through the assimilation of
379 the synthetic observations at the targeting time. Stations for EXP_sen_fixed_1cycle are located
380 in the sensitive area along the designed “Z” shape route (Figures 6a and 7). Stations for
381 EXP_tar_fixed_1cycle are located in the target region; these stations are parallel to the stations
382 of EXP_sen_fixed_1cycle, but the center of their route is located in the center of the target
383 region (Figure 7). The regionally averaged temperature profile RMSEs in the target region at the
384 verification time (26 August) between the natural run EXP0 and other experiments are used to
385 evaluate the benefit of the observations for thermal structure prediction.



386

387 **Figure 8.** Temporal evolution of the regionally-averaged temperature profile RMSEs in the
 388 target region during the prediction time in the Observing System Simulation Experiments.

389

390 The temporal evolutions of the temperature profile RMSEs in the OSSEs are shown in
 391 Figure 8. At the targeting time, the regionally averaged RMSEs in the target region are
 392 approximately 0.28°C for the control experiment (EXP_perturb) and attenuate to approximately
 393 0.235°C at the prediction time (the black line in Figure 8). Although the absolute magnitudes of
 394 the RMSEs in the OSSEs are small because of the small initial perturbations, the relative
 395 magnitudes of the RMSEs and their temporal evolution can still reflect the effectiveness of the
 396 different observation strategies. In the EXP_tar_fixed_1cycle, which represents the conventional
 397 observation strategy, the initial RMSEs are greatly reduced after data assimilation in the target
 398 region (the red dashed line in Figure 8). After 7 days of integration, the effectiveness of the
 399 forecast refinement decreases. In the EXP_sen_fixed_1cycle, the initial RMSEs are only slightly
 400 reduced at the targeting time (the red solid line in Figure 8) because only one of the total 12
 401 stations is located inside the target region. However, at the verification time, the forecast errors
 402 are smaller than the results of both EXP_perturb and EXP_tar_fixed_1cycle. These results

403 support the effectiveness of our observation strategy and data assimilation system.

404 To further reduce the forecast error, we explore the possibilities for improving the initial
405 state by utilizing the cycle data assimilation technique. In the EXP_sen_fixed_3cycles and
406 EXP_tar_fixed_3cycles, the data are cycle assimilated three times (00:00, 18, 19, 20 August) at
407 the fixed stations in the sensitive area and the target region, respectively (Figure 6a and Figure 7).
408 Compared to the one-time data assimilation (red solid and dashed lines in Figure 8), at the
409 targeting time, the initial RMSEs are both reduced by the corresponding three cycles of data
410 assimilation (green solid and dashed lines in Figure 8). After 7 days of integration, the forecast
411 errors in the EXP_sen_fixed_3cycles are minimal compared to those of both
412 EXP_tar_fixed_3cycles and EXP_sen_fixed_1cycle. This gives us confidence in the ability of
413 cycle data assimilation to reduce the forecast uncertainty in the identified sensitive area.

414 We realize that the locations of sensitive areas on 18 and 19 August (9 days and 8 days
415 before the verification time) may be different from that on 20 August (7 days before the
416 verification time). Thus, following the same procedure described in section 3.2, the 8-day, 9-day
417 and 10-day sensitive areas are identified, and these areas are shown in Figures 6b-d. The
418 centralis of the identified sensitive area moves northeastward and becomes oblate with increasing
419 prediction time. The previously designed stations based on the 7-day sensitive area are all out of
420 the range of the 10-day sensitive area (Figure 6d).

421 Then, new deployment locations based on the identified 8-day and 9-day sensitive areas are
422 designed following the same rule (Figures 6b and c). All the stations based on the 8-day and 9-
423 day sensitive areas are outside of the target region. The impact of the time-varying observation
424 stations is evaluated by conducting two extra experiments, EXP_sen_varied_3cycles and
425 EXP_tar_varied_3cycles. In EXP_sen_varied_3cycles, data are cycle assimilated three times
426 (00:00, 18, 19, 20 August) at the stations in the 7-day, 8-day and 9-day sensitive areas (see
427 station locations in Figures 1 and 7). In EXP_tar_varied_3cycles, the stations of
428 EXP_sen_varied_3cycles are moved parallel to the center of the target region (Figures 7 and
429 10d). At the targeting time, the RMSE of EXP_sen_varied_3cycles (the blue solid line in Figure
430 8) is larger than that of EXP_sen_fixed_3cycles because the designed stations based on the 8-day
431 and 9-day sensitive areas are farther away from the target region than those based on the 7-day
432 sensitive area. While the initial RMSE of EXP_tar_varied_3cycles (the blue dashed line in

433 Figure 8) is less than that of EXP_tar_fixed_3cycles because the designed stations based on the
 434 8-day and 9-day sensitive areas have broader spatial coverage than those based on the 7-day
 435 sensitive area. After 7 days of integration, EXP_sen_varied_3cycles performs the best among all
 436 the OSSEs in reducing the forecast error.

437 A two-cycle data assimilation experiment in the sensitive area is also conducted, and the
 438 forecast improvement falls between those of EXP_sen_fixed_1cycle and
 439 EXP_sen_varied_3cycles (not shown). Four-cycle data assimilation experiments are not
 440 implemented considering the actual observation cost in the field campaign. One may argue that,
 441 why not triple the observation stations from 12 to 36 in the one-time data assimilation in the
 442 sensitive area? In fact, as mentioned above, limited by the ship route length and the horizontal
 443 model resolution, a denser observation will not significantly expand the spatial observation
 444 coverage.

445 To further assess the effectiveness of the observation strategy in the subsequent field
 446 operation, we conduct additional OSSEs based on the simulated results of the hindcast years
 447 2016-2018 (Table 2). In every hindcast year, the hindcast control experiments are first created
 448 following the same procedures as those in EXP_perturb. Then, similar to
 449 EXP_sen_varied_3cycles and EXP_tar_varied_3cycles, the benefit of the targeted observation is
 450 tested through the assimilation of the synthetic observations at the time-varying stations in the
 451 sensitive areas and the target region, respectively. After 7 days of integration, in every hindcast
 452 year, assimilating data in the sensitive areas based on the above determined observation strategy
 453 can yield more profit than the conventional local data assimilation (Table 3). The results
 454 mentioned above support the implementation of the targeted observation campaign in the
 455 summer 2019 in the YS.

456 **Table 2.** Observing System Simulation Experiments based on the hindcast runs

Experiments	Comment
EXP2016	Nature run
EXP2016_perturb	Control run
EXP2016_tar_varied_3cycles	Three-times cycle assimilation in the target region at the time-varying stations

EXP2016_sen_varied_3cycles	Three-times cycle assimilation in the sensitive area at the time-varying stations
EXP2017	Nature run
EXP2017_perturb	Control run
EXP2017_tar_varied_3cycles	Three-times cycle assimilation in the target region at the time-varying stations
EXP2017_sen_varied_3cycles	Three-times cycle assimilation in the sensitive area at the time-varying stations
EXP2018	Nature run
EXP2018_perturb	Control run
EXP2018_tar_varied_3cycles	Three-times cycle assimilation in the target region at the time-varying stations
EXP2018_sen_varied_3cycles	Three-times cycle assimilation in the sensitive area at the time-varying stations

457

458 **Table 3.** Assessment of the designed observing strategy in the hindcast years of 2016-2018

459

(RMSEs refinement in percentage)

Experiments	Year	2016	2017	2018
	EXP_tar_varied_3cycles		-32.0%	20.3%
EXP_sen_varied_3cycles		43.9%	48.2%	70.1%

460

461 **4. Forecast improvements and discussion**462 **4.1 DATA**

463 A dedicated ocean survey with two synergetic ships is carried out in August 2019 to obtain
464 the targeted observation data in the YS. In the target region, five buoys (red crosses in Figure
465 10c) are placed from 17 to 27 August for forecast validation and OSEs. The buoys are composed
466 of temperature loggers (SBE56), pressure-temperature loggers (SBE39 and RBRduo³) and

467 pressure-temperature-conductivity loggers (RBRconcerto³), which can obtain the temperature
468 profiles of nearly the total water volume in approximately 2 m vertical bins. Both ends of the
469 buoys are equipped with pressure sensor instruments to determine the depths of the temperature
470 loggers between them. The sensors collected a sample every 10 mins. During 18-20 August, 21
471 temperature profiles are obtained by shipboard CTD (stars in Figure 10) to measure the influence
472 of local data assimilation in the target region on forecasts.

473 In the sensitive areas, temperature profiles are collected by the eXpendable
474 BathyThermographs (XBT) during 18-20 August. Temperature profiles at each XBT station are
475 detected four times a day (16:30-19:30, 22:30-1:30, 4:30-7:30, 10:30-13:30) along the
476 predesigned routes to obtain the daily averaged value, which are used in the cycle data
477 assimilation at 00:00 on 18, 19, and 20 August 2019. Given that the repeated cruises undergo
478 inevitable spatial uncertainty, after performing data quality control, the daily averaged
479 temperature profiles used for data assimilation are obtained by interpolating both the XBT data
480 and the simultaneous buoy data at the standard station locations. All times in the study are
481 referenced to the Chinese Standard Time (UTC+8).

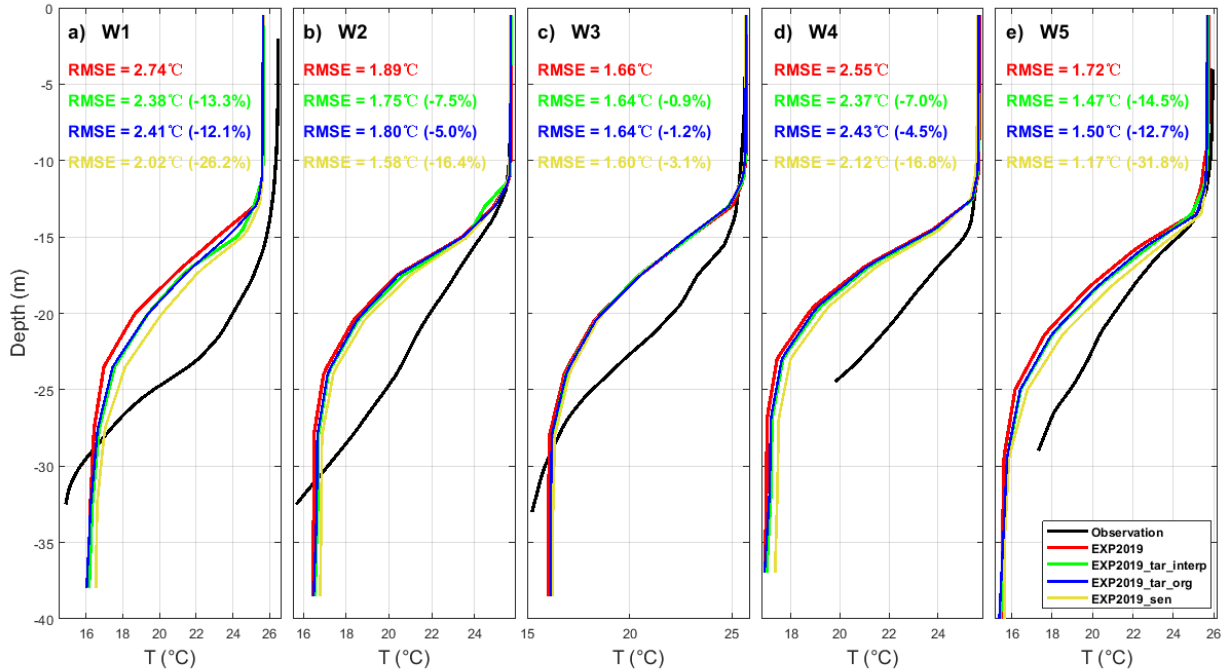
482 **4.2 Forecast improvements**

483 In this section, the performance of the targeted observations in improving the forecast is
484 validated. The daily-averaged temperature profiles of the model results and the observation data
485 at the five buoy stations in 26 August, 2019 are compared (Figure 9, see buoy locations in Figure
486 10c). The simulated sea surface temperature agrees very well with the observations, but the
487 predicted upper mixed layer thicknesses are slightly thinner. At the bottom, the simulated
488 temperature is higher than the observation, which may be caused by the insufficient cooling in
489 the previous winter. Compared to the upper and bottom layers, the accuracy in the middle water
490 volume is lower as a result of strong seasonal variations in the shallow sea thermocline, and the
491 predicted temperature was relatively lower. At the buoy stations, the RMSEs between the
492 modeled temperature profiles and the observations are approximately 1.66-2.74 °C (an average
493 value of 2.11 °C), and these errors increase to 2.26-3.75 °C (an average value of 2.84 °C) when
494 the depth ranges are restricted to the thermocline of 15-30 m. It should be noted that the
495 temperature RMSEs are only calculated at depths where observations are available. Horizontally,

496 the modeled temperature RMSEs at stations W1 and W4 are apparently higher than those at the
497 other three stations. This indicates that it is more difficult to correctly reproduce the summer
498 vertical thermal structures on the continental slopes with lesser water depths (Figure 10c).
499 Overall, the simulation successfully captures the general vertical thermal structures in the target
500 region, but there is still much room to improve the forecast accuracy, especially within the depth
501 range of the summer thermocline.

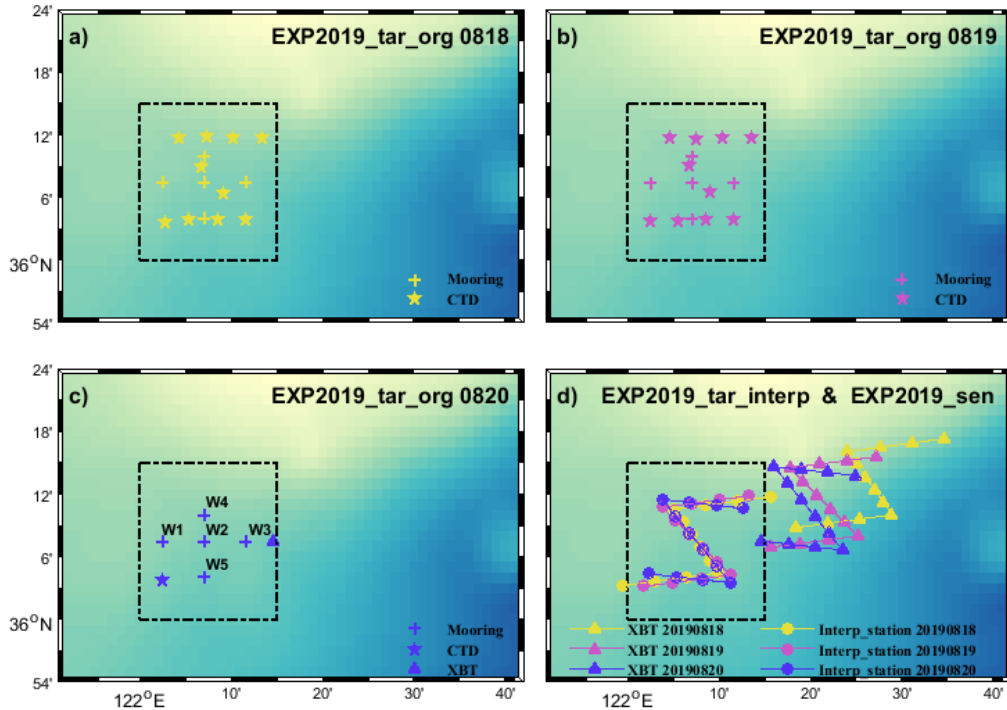
502 Then, observations obtained in the sensitive area are assimilated to quantify the benefits of
503 the targeted observations (EXP2019_sen). As illustrated in Figure 9, there is a marked
504 improvement in the vertical thermal structure simulations after assimilation. Among the five
505 buoy stations, the average RMSEs between the modeled temperature profiles and the
506 observations are reduced from 2.11 to 1.7 °C, with an average forecast improvement of
507 approximately 18.9% (compared to that of the EXP2019). However, one may argue that, this
508 significant forecast improvement could be attributed to the data assimilation technique rather
509 than the targeted observations. To highlight the contribution of the targeted observations, we
510 conduct a series of OSEs (Table 4) in the following section. The results show that the prediction
511 benefits decrease if the equivalent measurements are deployed locally in the target region.

512



513

514 **Figure 9.** Comparison of the observed and simulated daily-averaged temperature profiles at five
 515 buoys (see locations in Figure 10c). The black lines indicate the in-situ observations. The red
 516 lines indicate the model results without assimilation. The blue lines and the yellow lines indicate
 517 the improvement in the prediction from the assimilation of the observations in the target region
 518 and sensitive area, respectively. The green lines indicate the model results of
 519 EXP2019_tar_interp for the assimilation of the interpolated data at the synthetic stations in the
 520 target region (see locations in Figure 10d).



521

522 **Figure 10.** Station locations of the Observing System Experiments. The buoy stations, XBT
 523 stations, and shipboard CTD stations are denoted by the crosses, triangles and stars, respectively.
 524 The circles inside the target region in d) indicate the synthetic stations. The different deployment
 525 times of the observations are distinguished by different colors.

526

527

Table 4. Design of Observing System Experiments

Experiments	Data assimilation	Assimilation cycle	Comment
EXP2019	no	-	Control run
EXP2019_tar_org	yes	3	Cycle assimilate the original observations in the target region (15 profiles in 18 and 19 August, respectively, and 7 profiles in 20 August)
EXP2019_tar_interp	yes	3	Cycle assimilate the interpolated data at the synthetic stations in the target region (36 profiles)

EXP2019_sen	yes	3	Cycle assimilate the XBT data at the stations designed based on the identified 7-days, 8-days and 9-days sensitive areas, respectively (36 profiles)
-------------	-----	---	--

528

529

530 **4.3 Observing System Experiments**

531 The benefit of oceanic targeted observations has been tested in some previous studies
532 through a series of OSSEs (Li et al., 2014; Wang et al., 2013; Zhang et al., 2019). However, the
533 effect of oceanic targeted observations guided by sensitive areas has never been tested in OSEs
534 through the use of real data in actual operation. Generally, in the context of standard OSEs
535 designed for atmospheric targeted observation, the experiment assimilating all the available
536 observations is regarded as the control experiment, and the impact of the selected observations is
537 assessed by removing subsets of the measurements or by adding extra measurements and
538 comparing the results with the control experiment (Majumdar et al., 2011). In the oceanic region
539 of this study, the historical observations that we can obtained are sparse. Thus, we set an
540 experiment that does not assimilate any data as the control experiment (EXP2019). Given that
541 the target region is the most representative nonsensitive area for the benefit assessment of OSEs,
542 in addition to experiment EXP2019_sen, we conducted two extra experiments that assimilate
543 approximately equal amounts of measurements inside the target region: EXP2019_tar_org, for
544 which a total of 37 originally observed temperature profiles in the target region are assimilated
545 (see locations in Figures 10a-c), and EXP2019_tar_interp, for which 36 interpolated data in a set
546 of synthetic stations in the target region are assimilated (see locations in Figure 10d). These
547 synthetic stations are parallel to the corresponding stations in the sensitive area, but their daily
548 routes are located in the center of the target region. The daily averaged temperature profiles are
549 obtained by interpolating all the observations available on that day to the synthetic stations. It
550 should be noted that, to take full advantage of the limited observations, the shipboard CTD
551 temperature profiles used in the OSEs are only one-time measurements instead of daily averaged
552 values, which is a flaw of the designed OSEs.

553 Despite the difference in the spatial locations and numbers of the temperature profiles
 554 assimilated every day of the cycle assimilation, the forecast improvements in EXP2019_tar_org
 555 and EXP2019_tar_interp are nearly the same. In every buoy station, the simulated temperature
 556 profiles in EXP2019_tar_org and EXP2019_tar_interp are refined due to data assimilation in the
 557 target region. However, the forecast improvements in EXP2019_tar_org and
 558 EXP2019_tar_interp are both less than half of that in EXP2019_sen (average RMSE decreases of
 559 7.1% and 8.6% vs. 18.9%). The results of the OSEs support our initial assumption that
 560 conducting data assimilation in the CNOP-identified sensitive area is more effective in forecast
 561 improvement than in other areas including the target region itself. However, it should be noted
 562 that, the quantitative benefit of targeted observation in the CNOP-identified sensitive area differs
 563 from model to model and depends on the initial simulation accuracy and the selected data
 564 assimilation scheme.

565 **4.4 Dynamic analysis**

566 To better understand how the local forecast errors are efficiently reduced by conducting
 567 targeted observations in the remote sensitive area, it is worth exploring the dynamics behind. We
 568 quantitatively investigate the physical processes affecting the water temperature in the target
 569 region using the model temperature equation

$$570 \quad \frac{\partial T}{\partial t} = -\nabla \cdot (\vec{v}T) + \nabla_h (A_h \nabla_h T) + \frac{\partial}{\partial z} (A_v \frac{\partial T}{\partial z}), \quad (8)$$

571 where T is temperature, \vec{v} is velocity, and A_h and A_v are the horizontal and vertical diffusivity
 572 coefficients, respectively. The temperature change in the water is mainly induced by horizontal
 573 temperature advection, vertical temperature advection, horizontal temperature diffusion and
 574 vertical temperature diffusion. The ocean temperature is also affected by the change in surface
 575 heating. However, considering that in this study, we only conducted targeted observations inside
 576 the water volume, thus, only the impact of advection and diffusion processes are discussed.

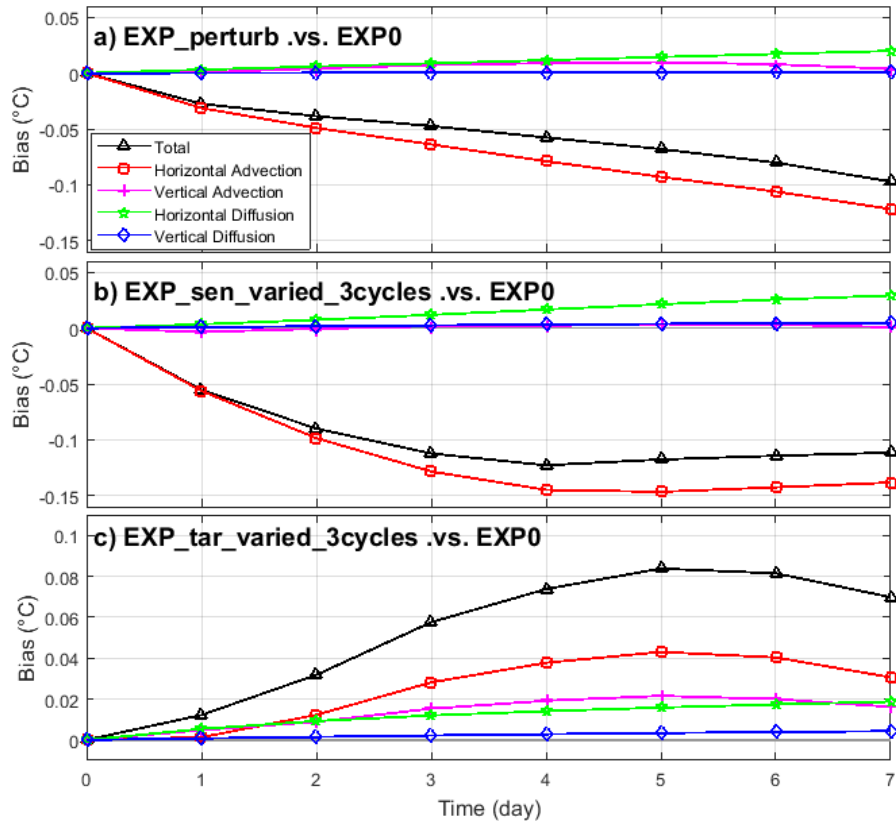
577 The temporal evolution of the vertically integrated and regionally averaged temperature
 578 biases induced by different processes in the target region is shown in Figure 11. Since we are
 579 focused on the evolution of different processes during the prediction time rather than the initial

580 refinement of the ocean state, the initial biases are set to zero at the targeting time. The total
581 biases of EXP_perturb and EXP_sen_varied_3cycles against EXP0 are always negative,
582 suggesting a decrease in the temperature discrepancy against the natural run, which is consistent
583 with the previous results of OSSEs (the black and blue descending trend lines in Figure 8).
584 However, the total biases of EXP_tar_varied_3cycles against EXP0 are positive, which suggests
585 that the temperature field in EXP_tar_varied_3cycles becomes worse since the targeting time
586 (the blue dashed line in Figure 8). Due to the effectiveness of the targeted observation, the
587 amplitude of the bias for EXP_sen_varied_3cycles against EXP0 is larger than that for
588 EXP_perturb against EXP0. Thus far, we can conclude that conventional local data assimilation
589 can greatly improve the initial temperature field in the target region, but the effectiveness
590 decreases during model integration. In contrast, the temperature field in the target region may not
591 be significantly refined through the assimilation of the data in the remote sensitive area at the
592 targeting moment, but it will be continuously improved during the prediction time, and reach a
593 more precise state at the verification time.

594 It is clear that the horizontal advection accounts for the majority of the temperature biases
595 during the prediction time (Figure 11). The temperature biases of vertical advection, horizontal
596 diffusion and vertical diffusion are always positive, indicating a negative effect of these three
597 processes. In Figures 11a and b, the temperature biases of horizontal advection have the largest
598 negative amplitude, suggesting that the horizontal temperature advection contributes the most to
599 improving the prediction. In EXP_tar_varied_3cycles, both the advection and diffusion processes
600 lead to a reduction in the simulation accuracy, within which the horizontal advection contributes
601 the most.

602 As the baroclinic response of the YSCWM, there exists a cyclonic gyre of approximately
603 0.2 Sv in the summer YS (Naimie et al., 2001). The identified sensitive area is located
604 northeastward of the target region, which is consistent with the local flow direction of the
605 YSCWM circulation (southwestward). From historical studies, although the YS summer
606 circulation was supposed to feature a complex two-layer or three-layer structure (Xu et al., 2002;
607 Xia et al., 2006), it is widely accepted that most of the middle water volume (4-40 m) is
608 dominated by a basin-scale cyclonic circulation. This interprets our results that the refinement of
609 the vertical thermal structures by targeted observation mainly occurs in the middle water volume

610 rather than in the surface or bottom mixed layer (Figure 9). Through the assimilation of the
 611 targeted measurements in the sensitive area, the information is subsequently advectively carried
 612 downstream to the target region by the YSCWM circulation. The distance of the identified
 613 sensitive area from the target region is associated with the involved prediction time.



614

615 **Figure 11.** Temporal evolution of the vertically-integrated regionally-averaged temperature
 616 biases induced by different processes in the target region for a) EXP_perturb vs. EXP0, b)
 617 EXP_sen_varied_3cycles vs. EXP0, and c) EXP_tar_varied_3cycles vs. EXP0 during the
 618 prediction time.

619 5. Conclusion

620 Targeted observation is believed to be a cost-effective way to decrease forecast uncertainty
 621 through the assimilation of additional measurements in the initial state. This study first extends
 622 the scope of oceanic targeted observations to the vertical thermal structure predictions. Given a

623 selected target region and a fixed prediction period of seven days, the sensitive areas are
624 identified utilizing the CNOP method and a newly defined objective function. The majority of
625 the sensitive areas are located outside of the target region in the northeast. Through the
626 superimposition of random errors in several selected regions, the initial state of the sensitive area
627 is proven to have the most impact on the thermal structure prediction in the target region. Given
628 that the locations of the identified sensitive areas in the hindcast and climatology runs are
629 generally consistent, guided by the CNOP-identified sensitive area of the last climatology year,
630 we design the observation strategy with the technique of cycle data assimilation and the new
631 concept of the time-varying sensitive area. A series of OSSEs are conducted to assess the
632 observation performance before the field campaign. The results show that, cycle assimilating
633 temperature profiles at the designed stations in the 7-day, 8-day and 9-day sensitive areas can
634 yield the maximum benefits.

635 A choreographed field campaign is then applied in the summer of 2019 in the YS to
636 evaluate the capabilities of targeted observations to reduce the temperature uncertainty in
637 numerical predictions. Our field experiment applied XBTs to purposefully sample the thermal
638 profiles in the sensitive areas. Inside the target region, an approximately equal number of
639 temperature profiles were gathered by shipboard CTDs and buoys. OSEs were conducted to test
640 the capabilities of targeted observations. The results show that reducing the initial errors in the
641 sensitive area can lead to improvement in the thermal structure prediction (18.9%) greater than
642 that in the target region (7-9%). Compared to assimilating local observations in the target region,
643 assimilating observations in the identified sensitive areas can double the benefit of data
644 assimilation regarding forecast improvements. To explore this further, we investigated the
645 physical dynamics behind. A term-by-term analysis of the model temperature equation indicates
646 that the horizontal temperature advection contributes the most to forecast improvement during
647 the prediction time. After conducting targeted observation in the upstream sensitive area, the
648 physical signals are subsequently carried downstream to the target region by the horizontal
649 temperature advection of the YSCWM circulation.

650 In this study, we skip the step of establishing a real-time prediction model, on the basis that
651 the locations of the identified sensitive areas in the hindcast and climatology runs are generally
652 consistent. Although this kind of spatial consistency was also found in the optimal precursor

653 study of the Kuroshio intrusion into the SCS (Liang et al., 2019; personal communication), it will
654 not always be applicable if the focused phenomenon or study area changes. Thus, future work
655 should be guided based on a reliable local prediction system. Furthermore, the optimal
656 deployment network should be investigated and extended to the three-dimensional scenarios. A
657 more advanced data assimilation technique is also needed to better exploit the targeted data.

658 **Acknowledgments**

659 This paper benefited from the insightful and constructive comments of the journal editor and the
660 anonymous reviewers. We would like to thank the use of super computer for all the numerical
661 simulations at the Navy Submarine Academy Underwater Marine Environment Institute. We are
662 also gratefully acknowledge to the captains Bing Liu and Xiufeng Chen, the laboratory director
663 Lei Chen, and all the crews of the R/V KeXue No.3 and R/V ChuangXin No.2 for their help in
664 collecting the data. The ETOPO2 topography is available at the website
665 (<https://ngdc.noaa.gov/mgg/global/etopo2>). The HYCOM+NCODA reanalysis data is available
666 at the website (<https://www.hycom.org/dataserver>). The ECMWF atmosphere forcing data is
667 available at the website (<https://apps.ecmwf.int/datasets/>). The TPXO7.2 tidal forcing can be
668 obtained from the website (<https://www.tpxo.net>). The observation data can be downloaded
669 from the website (<https://figshare.com/s/f486e3452e731f6a8a70>). This work was supported by
670 funds from the National Natural Science Foundation of China (Grants No. 41906005 & No.
671 41705081), National Basic Research Program of China (Grant No. 2019-JCJQ-ZD-149-00),
672 Innovation Special Zone Project (Grant No. 18-H863-05-ZT-001-012-06), and the Laboratory
673 for Regional Oceanography and Numerical Modeling, Qingdao National Laboratory for Marine
674 Science and Technology (Grant NO. 2019A05). K. Liu and G. Wu contributed equally to this
675 work.

676 **References**

677 Alvarez, A., & Mourre, B. (2012). Optimum sampling designs for a glider-mooring
678 observing network. *J. Atmos. Oceanic Technol.*, 29(4), 601-612, doi.org/ 10.1175/JTECH-D-11-
679 00105.1

680 Baehr, J., Mcinerney, D., Keller, K., & Marotzke, J. (2008). Optimization of an observing
681 system design for the North Atlantic Meridional Overturning Circulation. *J. Atmos. Oceanic*
682 *Technol.*, 25(4), 625-634, doi.org/ 10.1175/2007jtecho535.1

683 Chen, G., Niu, Y., Wen, S., Bao, C., Guan, D., Wu, B., et al. (1992). Marine atlas of Bohai
684 Sea, Yellow Sea, East China Sea (Hydrology). China Ocean Press, Beijing, China.

685 Curtin, T. B., & Bellingham, J. G. (2009). Progress toward autonomous ocean sampling
686 networks. *Deep Sea Res., Part II: Topical Studies in Oceanography*, 56(3-5), 0-67, doi.org/
687 10.1016/j.dsr2.2008.09.005

688 Duan, W., & Hu, J. (2016). The initial errors that induce a significant “spring predictability
689 barrier” for El Niño events and their implications for target observation: results from an earth
690 system model. *Clim. Dynam.*, 46, 3599-3615, doi.org/10.1007/s00382-015-2789-5

691 Dushaw, B. D., Worcester, P. F., Dzieciuch, M. A., & Menemenlis, D. (2013). On the time-
692 mean state of ocean models and the properties of long range acoustic propagation. *J. Geophys.*
693 *Res.*, 118(9), 4346-4362, doi.org/ 10.1002/jgrc.20325

694 Egbert, G. D., & Erofeeva, S. Y. (2002). Efficient inverse modeling of barotropic ocean
695 tides. *J. Atmos. Oceanic Technol.*, 19, 183-204, doi.org/ 10.1175/1520-
696 0426(2002)019<0183:EIMOBO>2.0.CO;2

697 Farrara, J. D., Chao, Y., Li, Z., Wang, X., Jin, X., Zhang, H., et al. (2013). A data-
698 assimilative ocean forecasting system for the Prince William sound and an evaluation of its
699 performance during sound Predictions 2009, *Cont. Shelf Res.*, 63, S193–S208,
700 doi.org/10.1016/j.csr.2012.11.008

701 Flather, R. A. (1976). A tidal model of the north-west European continental shelf. *Mem.*
702 *Soc. Roy. Sci. Liege*, 6, 141-164.

703 Hu, D., & Wang, Q. (2004). Interannual variability of the southern Yellow Sea Cold Water
704 Mass. *Chin. J. Oceanol. Limn.*, 22(3), 231-236, doi.org/10.1007/BF02842553

- 705 Ji, X., Kwon, K. M., Choi, B.-J., Liu, G., Park, K.-S., Wang, H., et al. (2017). Assimilating
706 OSTIA SST into regional modeling systems for the Yellow Sea using ensemble methods. *Acta*
707 *Oceanolo. Sin.*, 36(3), 37–51, doi: 10.1007/s13131-017-0978-2
- 708 Köhl, A., & Stammer, D. (2004). Optimal observations for variational data assimilation. *J.*
709 *Phys. Oceanogr.*, 34(3), 34-42, doi.org/ 10.1175/2513.1
- 710 Kramer, W., Dijkstra, H. A., Pierini, S., & Leeuwen, P. J. V. (2012). Measuring the impact
711 of observations on the predictability of the Kuroshio Extension in a shallow-water model. *J.*
712 *Phys. Oceanogr.*, 42(1), 3-17, doi.org/10.1175/JPO-D-11-014.1
- 713 Large, W. G., McWilliams, J. C., & Doney, S. C. (1994). Oceanic vertical mixing: A review
714 and a model with a nonlocal boundary layer parameterization. *Rev. Geophys.*, 32, 363-403,
715 doi.org/10.1029/94rg01872
- 716 Lermusiaux, P. F. J. (2007). Adaptive modeling, adaptive data assimilation and adaptive
717 sampling. *Physica. D.*, 230(1-2), 172-196, doi.org/ 10.1016/j.physd.2007.02.014
- 718 Li, Y., Peng, S., & Liu, D. (2014). Adaptive observation in the South China Sea using
719 CNOP approach based on a 3-D ocean circulation model and its adjoint model. *J. Geophys. Res.*,
720 119(12), 8973-8986, doi.org/10.1002/2014JC010220
- 721 Liang, P., Mu, M., Wang, Q., & Yang, L. (2019). Optimal precursors triggering the
722 Kuroshio Intrusion into the South China Sea obtained by the Conditional Nonlinear Optimal
723 Perturbation approach. *J. Geophys. Res.*, 124, 3941-3962, doi.org/10.1029/2018JC014545
- 724 Liu, K., Sun, J., Guo, C., Yang, Y., Yu, W., & Wei, Z. (2019). Seasonal and spatial
725 variations of the M2 internal tide in the Yellow Sea. *J. Geophys. Res.*, 124,
726 doi.org/10.1029/2018JC014819
- 727 Majumdar, S. J., Abernethy, S. D., Bishop, C. H., Cardinali, C., Caughey, J., Doerenbecher,
728 A., et al. (2011). Targeted observations for improving numerical weather prediction: An
729 overview. *WWRP/THORPEX Publ.* 15, 37 pp.
730 https://www.wmo.int/pages/prog/arep/wwrp/new/documents/THORPEX_No_15.pdf

- 731 Majumdar, S. J. (2016). A Review of Targeted Observations. *B. Am. Meteorol. Soc.*,
732 97(12), doi.org/ 10.1175/BAMS-D-14-00259.1
- 733 Montani, A., Thorpe, A. J., Buizza, R., & Uden, P. (1999). Forecast skill of the ECMWF
734 model using targeted observations during FASTEX. *Q. J. R. Meteorol. Soc.*, 125, 3219-3240,
735 doi.org/10.1002/qj.49712556106
- 736 Morss, R. E., & Battisti, D. S. (2004). Evaluating observing requirements for ENSO
737 prediction: experiments with an intermediate coupled model. *J. Climate*, 17(16), 3057-3073,
738 doi.org/10.1175/1520-0442(2004)017<3057:eorfep>2.0.co;2
- 739 Mourre, B., & Alvarez, A. (2012). Benefit assessment of glider adaptive sampling in the
740 Ligurian Sea. *Deep Sea Res., Part I*, 68, 68-78, doi.org/ 10.1016/j.dsr.2012.05.010
- 741 Mu, M., Duan, W., & Wang, B. (2003). Conditional Nonlinear Optimal Perturbation and its
742 applications. *Nonlinear Proc. Geoph.*, 10(6), 493-501, doi.org/10.5194/npg-10-493-2003
- 743 Mu, M., Zhou, F., & Wang, H. (2009). A method for identifying the sensitive areas in
744 targeted observations for tropical cyclone prediction: Conditional Nonlinear Optimal
745 Perturbation. *Mon. Weather Rev.*, 137(5), 1623-1639, doi.org/10.1175/2008mwr2640.1
- 746 Mu, M., Wansuo, D., & Tang, Y. (2017). The predictability of atmospheric and oceanic
747 motions: Retrospect and prospects. *Sci. China (Earth Sci.)*, 11, 97-108, doi.org/10.1007/s11430-
748 016-9101-x
- 749 Naimie, C. E., Blain, C. A., & Lynch, D. R. (2001). Seasonal mean circulation in the
750 Yellow Sea - a model-generated climatology. *Cont. Shelf Res.*, 21, 667-695, doi.org/
751 10.1016/s0278-4343(00)00102-3
- 752 Oke, P. R., Larnicol, G., Jones, E. M., Kourafalou, V., Sperrevik, A. K., Carse, F., et al.
753 (2015). Assessing the impact of observations on ocean forecasts and reanalyses: Part 2, Regional
754 applications. *J. Oper. Oceanogr.*, 8:sup1, s63-s79, doi.org/10.1080/1755876X.2015.1022080
- 755 Powell, M. J. D. (1983). VMCWD: A FORTRAN subroutine for constrained optimization.
756 *ACM SIGMAP Bulletin*, 32, 4-16, doi.org/10.1145/1111272.1111273

- 757 Shay, L. K., Jaimes, B., Brewster, J. K., Meyers, P., McCaskill, E., C., Uhlhorn, E., et al.
758 (2011). Airborne ocean surveys of the loop current complex from NOAA WP-3D in support of
759 the deepwater horizon oil spill. *Geophysical Monograph Series*, 195(10), 131-151,
760 doi.org/10.1029/2011GM001101
- 761 Shchepetkin, A. F., & McWilliams, J. C. (2005). The regional oceanic modeling system
762 (ROMS): A split-explicit, free-surface, topography-following-coordinate oceanic model. *Ocean*
763 *Model.*, 9, 347-404, doi.org/10.1016/j.ocemod.2004.08.002.
- 764 Wang, Q., Mu, M., & Dijkstra, H. A. (2013). The similarity between optimal precursor and
765 optimally growing initial error in prediction of Kuroshio large meander and its application to
766 targeted observation. *J. Geophys. Res.*, 118(2), 869-884, doi.org/ 10.1002/jgrc.20084
- 767 Wang, B., & Tan, X. (2009). A fast algorithm for solving CNOP and associated target
768 observation tests. *J. Meteorol. Res.*, 23(4), 387-402, doi.org/ 10.1016/j.agrformet.2009.02.014
- 769 Xia, C., Qiao, F., Yang, Y., Ma, J., & Yuan, Y. (2006). Three-dimensional structure of the
770 summer circulation in the Yellow Sea from a wave-tide circulation coupled model. *J. Geophys.*
771 *Res.*, 111, C11S03, doi.org/10.1029/2005JC003218.
- 772 Xu, D., Yuan, Y., & Liu, Y. (2002). The baroclinic current structure of Yellow Sea Cold
773 Mass. *Sci. China Ser. D*, 46(2), 117-126, doi.org/ 10.1360/03yd9011
- 774 Yang, D., Yin, B., Liu, Z., & Feng, X. (2011). Numerical study of the ocean circulation on
775 the East China Sea shelf and a Kuroshio bottom branch northeast of Taiwan in summer. *J.*
776 *Geophys. Res.*, 116, C05015, doi.org/10.1029/2010JC006777.
- 777 Zhang, K., Mu, M., & Wang, Q. (2017). Identifying the sensitive area in adaptive
778 observation for predicting the upstream Kuroshio transport variation in a 3-D ocean model. *Sci.*
779 *China (Earth Sci.)*, (05), 62-71, doi.org/CNKI:SUN:JDXG.0.2017-05-004
- 780 Zhang, K., Mu, M., Wang, Q., Yin, B., & Liu, S. (2019). CNOP-based adaptive observation
781 network designed for improving upstream Kuroshio transport prediction. *J. Geophys. Res.*, 124,
782 4350-4364, doi.org/10.1029/2018JC014490

783 Zhang, S., Wang, Q., Lü, Y., Cui, H., & Yuan, Y. (2008). Observation of the seasonal
784 evolution of the Yellow Sea Cold Water Mass in 1996-1998. *Cont. Shelf Res.*, 28(3), 442-457,
785 doi.org/10.1016/j.csr.2007.10.002